The Astrophysical Journal, 974:31 (8pp), 2024 October 10 https://doi.org/10.3847/1538-4357/ad6dd6

TESS Asteroseismology of β Hydri: A Subgiant with a Born-again Dynamo

Travis S. Metcalfe[1], Jennifer L. van Saders[2], Daniel Huber[2,3], Derek Buzasi[4], Rafael A. García[5], Keivan G. Stassun[6], Sarbani Basu[7], Sylvain N. Breton[8], Zachary R. Claytor[9,10], Enrico Corsaro[8], Martin B. Nielsen[11], J. M. Joel Ong[2,13], Nicholas Saunders[2,14], Amalie Stokholm[11,12], and Timothy R. Bedding[3]
[1] Center for Solar-Stellar Connections, White Dwarf Research Corporation, 9020 Brumm Trail, Golden, CO 80403, USA
[2] Institute for Astronomy, University of Hawai'i, 2680 Woodlawn Drive, Honolulu, HI 96822, USA
[3] Sydney Institute for Astronomy (SIfA), School of Physics, University of Sydney, Camperdown, NSW 2006, Australia
[4] Department of Chemistry and Physics, Florida Gulf Coast University, 10501 FGCU Boulevard S, Fort Myers, FL 33965, USA
[5] Université Paris-Saclay, Université Paris Cité, CEA, CNRS, AIM, 91191, Gif-sur-Yvette, France
[6] Department of Physics and Astronomy, Vanderbilt University, Nashville, TN 37235, USA
[7] Department of Astronomy, Yale University, PO Box 208101, New Haven, CT 06520-8101, USA
[8] INAF—Osservatorio Astrofisico di Catania, Via S. Sofia, 78, 95123 Catania, Italy
[9] Department of Astronomy, University of Florida, 211 Bryant Space Science Center, Gainesville, FL 32611, USA
[10] Space Telescope Science Institute, 3700 San Martin Drive, Baltimore, MD 21218, USA
[11] School of Physics & Astronomy, University of Birmingham, Edgbaston, Birmingham B15 2TT, UK
[12] Stellar Astrophysics Centre, Aarhus University, Ny Munkegade 120, DK-8000 Aarhus C, Denmark
Received 2024 June 18; revised 2024 August 7; accepted 2024 August 8; published 2024 October 3

Abstract

The solar-type subgiant β Hyi has long been studied as an old analog of the Sun. Although the rotation period has never been measured directly, it was estimated to be near 27 days. As a Southern Hemisphere target, it was not monitored by long-term stellar activity surveys, but archival International Ultraviolet Explorer data revealed a 12 yr activity cycle. Previous ground-based asteroseismology suggested that the star is slightly more massive and substantially larger and older than the Sun, so the similarity of both the rotation rate and the activity cycle period to solar values is perplexing. We use two months of precise time-series photometry from the Transiting Exoplanet Survey Satellite to detect solar-like oscillations in β Hyi and determine the fundamental stellar properties from asteroseismic modeling. We also obtain a direct measurement of the rotation period, which was previously estimated from an ultraviolet activity–rotation relation. We then use rotational evolution modeling to predict the rotation period expected from either standard spin-down or weakened magnetic braking (WMB). We conclude that the rotation period of β Hyi is consistent with WMB and that changes in stellar structure on the subgiant branch can reinvigorate the large-scale dynamo and briefly sustain magnetic activity cycles. Our results support the existence of a "born-again" dynamo in evolved subgiants—previously suggested to explain the cycle in 94 Aqr Aa—which can best be understood within the WMB scenario.

Unified Astronomy Thesaurus concepts: Stellar activity (1580); Stellar evolution (1599); Stellar oscillations (1617); Stellar rotation (1629)

1. Introduction

The solar-type subgiant β Hyi (HD 2151, TIC 267211065) has been studied for decades as an old analog of the Sun (D. Dravins et al. 1993a, 1993b, 1993c, 1998). Some of the earliest attempts to detect solar-like oscillations only produced upper limits (S. Frandsen 1987; P. D. Edmonds & L. E. Cram 1995), but high-precision radial velocity measurements ultimately identified excess power around 1 mHz (T. R. Bedding et al. 2001; F. Carrier et al. 2001), and a subsequent dual-site campaign resolved the individual mode frequencies (T. R. Bedding et al. 2007). These observations led to some initial asteroseismic modeling of the global properties (M. P. Di Mauro et al. 2003; J. Fernandes & M. J. P. F. G. Monteiro 2003), followed by more precise modeling of the individual oscillation frequencies (G. Doğan et al. 2010; I. M. Brandão et al. 2011), revealing a star that is slightly more massive and substantially larger and older than the Sun.

As a Southern Hemisphere target, β Hyi was not monitored by the Mount Wilson survey, but archival International Ultraviolet Explorer (IUE) data revealed a 12 yr activity cycle (T. S. Metcalfe et al. 2007; see Figure 1). These same IUE observations were later used to estimate the rotation period ($P_{\rm rot}$), adopting an ultraviolet activity–rotation relation established from a larger sample of stars ($P_{\rm rot} = 27.1 \pm 1.7$ days; M. Olmedo et al. 2013). Activity cycles are rare in subgiants, with most of the evolved stars in the Mount Wilson survey showing constant activity over decades (S. L. Baliunas et al. 1995). The only two unambiguous examples of subgiants with cycling activity include HD 81809 (R. Egeland 2018) and 94 Aqr Aa (HD 219834A; T. S. Metcalfe et al. 2020), which are both members of binary or multiple star systems. The rotation and cycle period ($P_{\rm cyc}$) of HD 81809 places it near the short-period sequence of stellar activity cycles (E. Böhm-Vitense 2007; A. Brandenburg et al. 2017), while both 94 Aqr Aa and β Hyi appear to be outliers in a $P_{\rm rot}$ versus $P_{\rm cyc}$ diagram.

We use recent observations from the Transiting Exoplanet Survey Satellite (TESS; G. R. Ricker et al. 2014) to constrain the global properties of β Hyi and investigate the possible origins of its activity cycle. In Section 2, we describe the TESS

[13] NASA Hubble Fellow.
[14] NSF Graduate Research Fellow.

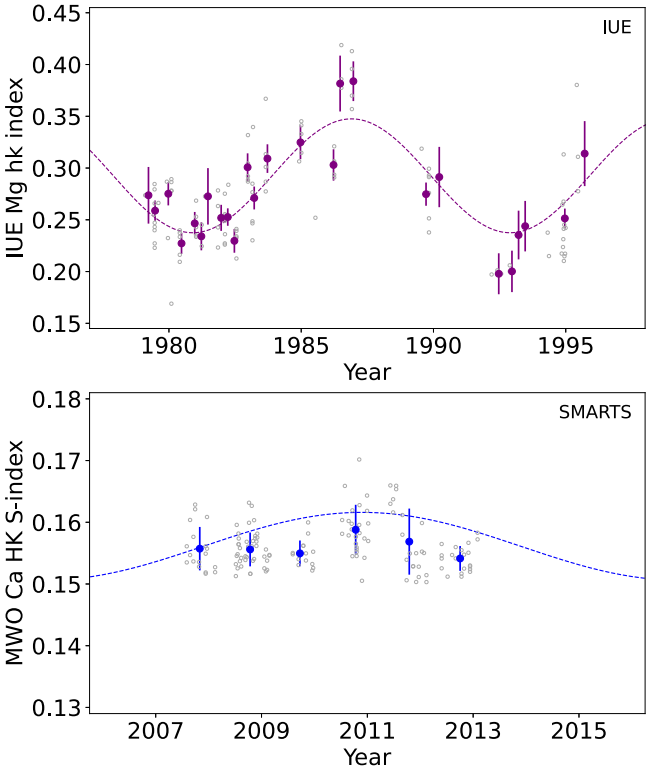

Figure 1. Activity cycle of β Hyi from IUE data (top, adapted from T. S. Metcalfe et al. 2007) and from ground-based observations (bottom). The horizontal and vertical scales of the two panels differ by factors of 2 and 6, respectively. Fractional variability due to the cycle is about 6 times larger in the ultraviolet than in the optical.

observations, and we derive new constraints on both the rotation period and the stellar luminosity. In Section 3, we analyze the TESS data to extract the solar-like oscillation frequencies, and we determine the fundamental stellar properties from asteroseismic modeling. In Section 4, we use rotational evolution models to probe standard spin-down and weakened magnetic braking (WMB) scenarios, and we propose that changes in stellar structure on the subgiant branch can reinvigorate the large-scale dynamo and briefly sustain magnetic activity cycles. Finally, in Section 5, we summarize and discuss our results, concluding that "born-again" dynamos in evolved subgiants can best be understood within the WMB scenario.

2. Observations

2.1. TESS Photometry

TESS observed β Hyi at 20 s cadence during Sectors 67 and 68, corresponding to 2023 July 1–2023 August 25, with the usual gaps midsector and between sectors for data downlink. We used 20 s instead of 2 minute data due to the significant improvement in photometric precision for bright stars (D. Huber et al. 2022). Given the brightness of β Hyi (Tmag = 2.216), we anticipated count rates of approximately $2 \times 10^7\,\mathrm{s}^{-1}$, which is consistent with the rates seen in the Science Processing Operations Center (SPOC; J. M. Jenkins et al. 2016) simple aperture photometry (SAP) light curves for both sectors. However, the corrected SPOC Pre-search Data Conditioning SAP (PDCSAP) light curve for both sectors shows a mean value of approximately $1.14 \times 10^7\,\mathrm{s}^{-1}$, substantially lower than both expectations and the uncorrected

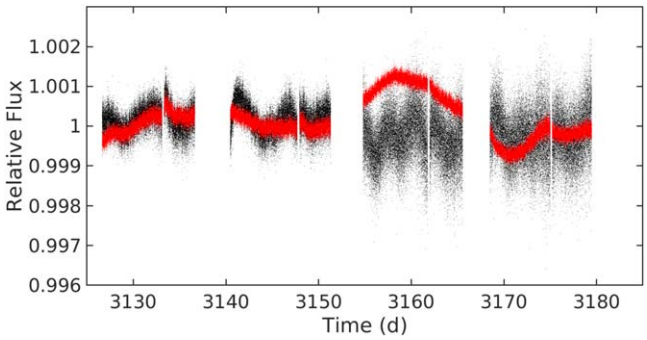

Figure 2. Light curves for β Hyi from TESS data. Red points show the unfiltered light curve described in Section 2.1, compared to the PDCSAP light curve in black. Our procedure reduces the rms noise level of the light curve by approximately a factor of 2.

version. Both SPOC light curves also show noise levels that are significantly higher than anticipated for such a bright star.

From experience, we know that the normal TESS data processing can struggle with bright sources such as β Hyi. Accordingly, we followed the procedures described in M. B. Nielsen et al. (2020) and T. S. Metcalfe et al. (2023a) to extract custom light curves for each sector. In essence, our aperture masks are created by starting from the pixel with the largest flux and adding additional pixels one at a time until the signal-to-noise ratio (S/N) no longer improves. The resulting light curve is then detrended against centroid pixel coordinates and high-pass filtered with a cutoff frequency of 100 μHz to minimize residual contributions from spacecraft positional jitter. Figure 2 compares our unfiltered light curve (red) to the PDCSAP data product (black), showing the approximately factor of 2 reduction in the rms noise level of the light curve.

2.2. Signatures of Rotation

To look for any signature of rotation in the unfiltered light curve described in Section 2.1, we started by interpolating the gaps with inpainting techniques based in a sparsity prior (M. Elad et al. 2005) using a multiscale discrete cosine transform (J.-L. Starck & F. Murtagh 2006; R. A. García et al. 2014b; S. Pires et al. 2015). This procedure has been successfully applied to determine the surface rotation periods of main-sequence stars, subgiants, and red giants (e.g., A. R. G. Santos et al. 2019, 2021; K. W. F. Lam et al. 2021; R. A. García et al. 2023). The resulting light curve was rebinned by 100 points to a final cadence of ~33 minutes.

The rotation period estimate was obtained from three different but complementary methods, which are illustrated in Figure 3. The initial method involved a period-time analysis (top left panel), using a Morlet wavelet–based decomposition (C. Torrence & G. P. Compo 1998). We projected the results onto the period axis, creating the global wavelet power spectrum (GWPS; S. Mathur et al. 2010; R. A. García et al. 2014a). Starting from the highest peak, we iteratively fit Gaussian functions (green line, top right panel) and subtracted them from the GWPS until no further power remained. The central value of the tallest Gaussian function serves as our initial estimate of $P_{\rm rot}$. We adopt the full width at half maximum as the measurement uncertainty—a conservative approach that considers the possibility of surface latitudinal differential rotation. A second estimate of $P_{\rm rot}$ was obtained from the autocorrelation function (ACF; A. McQuillan et al. 2013) of the light curve (middle panel). Finally, we multiplied

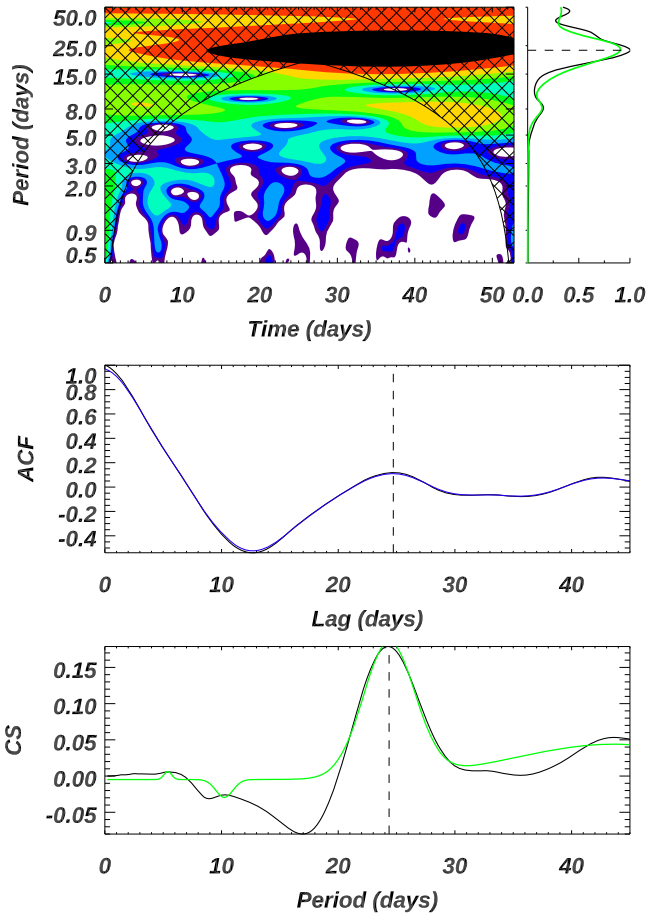

Figure 3. Analysis of the TESS light curve to determine $P_{\rm rot}$, including a period-time analysis (top left) projected onto the period axis and normalized by the maximum power (top right), an autocorrelation analysis (middle), and the CS (bottom). The hashed region in the top panel corresponds to the area where the retrieved periods are less reliable. Green lines correspond to the Gaussian fits (see Section 2.2 for details).

the GWPS and the ACF to obtain the composite spectrum (CS; T. Ceillier et al. 2016, 2017), which emphasizes signals common to both analyzes (bottom panel).

After benchmarking several different surface rotation pipelines, S. Aigrain et al. (2015) showed that combining different analysis techniques is a powerful method to determine a reliable value of $P_{\rm rot}$. Starting with the GWPS, the main periodicity corresponds to ∼23 days. Unfortunately, this value falls within the exclusion cone of the wavelet analysis, indicated by the hashed region in the top left panel of Figure 3. Reliable results typically require a light curve longer than 3 times the rotation period. The ACF shows a signal around 24.7 days, which is further enhanced in the CS (24.4 days). Given the star's brightness, we believe that the modulation is likely of stellar origin. Based on the current TESS data analysis, we conclude that the rotation period is $P_{\rm rot} = 23.0 \pm 2.8$ days. However, additional observations may be required to confirm this estimate. Note that previous single-sector data do not provide useful constraints.

2.3. Spectral Energy Distribution

To obtain a constraint on the stellar luminosity, we performed an analysis of the broadband spectral energy distribution (SED) of β Hyi together with the Gaia DR3 parallax, following the procedures described in K. G. Stassun & G. Torres (2016) and K. G. Stassun et al. (2017, 2018). No systematic offset was applied (see, e.g., K. G. Stassun & G. Torres 2021). We adopted the JHK_S magnitudes from 2MASS, the W3–W4 magnitudes from WISE, the *UBV* magnitudes from J. C. Mermilliod (2006), and the Strömgren *ubvy* magnitudes from E. Paunzen (2015). Together, the available photometry spans the full stellar SED over the wavelength range 0.4–20 μm.

We performed a fit using Kurucz stellar atmosphere models, with the effective temperature ($T_{\rm eff}$) from J. R. North et al. (2007) and the surface gravity ($\log g$) and metallicity ([Fe/H]) from H. Bruntt et al. (2010). The extinction A_V was fixed at 0 due to the very close proximity of the star ($d = 7.5$ pc). The resulting fit has a reduced χ^2 of 0.9. Integrating the model SED gives the bolometric flux at Earth, $F_{\rm bol} = 1.979 \pm 0.059 \times 10^{-6}$ erg s^{-1} cm^{-2}. Taking $F_{\rm bol}$ together with the Gaia parallax (Gaia Collaboration et al. 2021) yields the bolometric luminosity $L_{\rm bol} = 3.45 \pm 0.10\, L_\odot$.

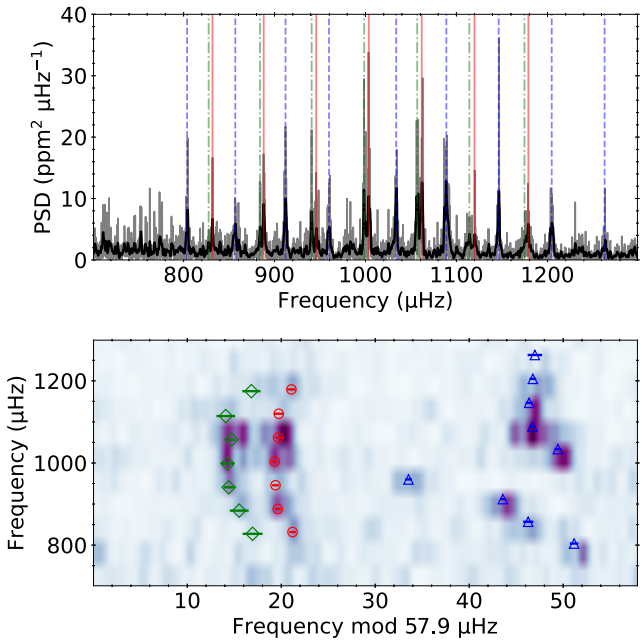

Figure 4. Power spectrum (top) and échelle diagram (bottom) centered on the power excess due to solar-like oscillations detected in β Hyi. Red solid lines and circles indicate extracted radial ($l = 0$) modes, blue dashed lines and triangles show extracted dipole ($l = 1$) modes, and green dashed–dotted lines and diamonds show extracted quadrupole ($l = 2$) modes.

3. Asteroseismology

3.1. Solar-like Oscillation Frequencies

The power spectrum of the filtered TESS light curve for β Hyi is shown in the top panel of Figure 4. We observe a clear series of regularly spaced peaks centered at a frequency near $\nu_{\rm max} = 1038$ μHz, consistent with previous detections of solar-like oscillations. To extract individual frequencies, three teams applied Lorentzian mode–profile fitting (e.g., R. A. García et al. 2009; R. Handberg & T. L. Campante 2011; T. Appourchaux et al. 2012; B. Mosser et al. 2012; E. Corsaro & J. De Ridder 2014; E. Corsaro et al. 2020; M. B. Nielsen et al. 2021; S. N. Breton et al. 2022). For each mode, we required two independent methods to return the same frequency within uncertainties. The consensus list of frequencies was further refined from visual inspection of the power spectrum. For the

Table 1
Identified Oscillation Frequencies for β Hyi

ν (μHz)	σ_ν (μHz)	l
803.86	0.46	1
827.55	1.06	2
831.80	0.36	0
856.87	0.54	1
884.02	1.00	2
888.13	0.35	0
912.08	0.29	1
940.81	0.54	2
945.79	0.36	0
959.94	0.37	1
998.59	0.61	2
1003.61	0.37	0
1033.74	0.37	1
1056.88	0.44	2
1061.86	0.37	0
1088.93	0.35	1
1114.19	0.99	2
1119.83	0.50	0
1146.47	0.37	1
1174.82	0.97	2
1179.08	0.45	0
1204.77	0.35	1
1262.89	0.77	1

final list, we adopted values from a single method, with uncertainties derived by adding in quadrature the median formal uncertainty and the standard deviation of the extracted frequencies from all methods that identified a given mode. Table 1 lists the identified frequencies, which agree with the corresponding modes from T. R. Bedding et al. (2007) within the uncertainties.

The bottom panel of Figure 4 shows an échelle diagram with a large separation of $\Delta\nu = 57.9$ μHz and the extracted frequencies. We identified seven radial ($l = 0$), nine dipole ($l = 1$), and seven quadrupole ($l = 2$) modes. The dipole modes show a clear avoided crossing near 950 μHz, a departure from the regular frequency spacing due to the interaction of gravity modes in the core and pressure modes in the envelope (M. Aizenman et al. 1977). Avoided crossings are often found in the oscillations of subgiants and are a powerful diagnostic of the stellar age (e.g., O. Benomar et al. 2012).

3.2. Asteroseismic Modeling

To determine the fundamental properties of β Hyi, several modeling teams attempted to match the oscillation frequencies identified in Section 3.1, along with the $T_{\rm eff}$ from J. R. North et al. (2007) and the [Fe/H] from H. Bruntt et al. (2010) with errors inflated to account for the systematic noise floor suggested by G. Torres et al. (2012), as well as the luminosity constraint from Section 2.3. The five independent analyzes used stellar evolution models from ASTEC (J. Christensen-Dalsgaard 2008a), GARSTEC (V. Aguirre Børsen-Koch et al. 2022), MESA (B. Paxton et al. 2011), and YREC (P. Demarque et al. 2008). The resulting determinations of the stellar properties were in very good agreement, with a relative dispersion of 2% in radius (1.796–1.840 $R_\odot$), 6% in mass (1.059–1.127 $M_\odot$), and 22% in age (6.1–7.5 Gyr). For consistency with the rotational evolution modeling in Section 4.1, below we provide additional details about the results from YREC and MESA (Asteroseismic Modeling Portal, AMP, 2.0; T. S. Metcalfe et al. 2023c).

The asteroseismic modeling with YREC generally followed the same procedures described in T. S. Metcalfe et al. (2020) for the subgiant 94 Aqr Aa. However, the characteristics of the model grids were different for β Hyi, and the treatment of spectroscopic constraints was modified slightly. The initial model grid for β Hyi was constructed with masses between 1.02 and 1.20 $M_\odot$ in increments of 0.01 $M_\odot$, initial helium abundances between 0.25 and 0.29, initial [Fe/H] between -0.15 and $+0.15$, and a mixing-length parameter between 1.4 and 2.1. After evaluating the most likely mass, a finer grid was constructed with masses between 1.09 and 1.12 $M_\odot$ and increments of 0.005 $M_\odot$, with all other parameters spanning the same ranges as in the initial grid. This finer grid was then used for a Monte Carlo analysis of the spectroscopic parameters. For each realization of the spectroscopic constraints, the most likely asteroseismic model was identified. The final stellar properties were obtained from the distribution of the most likely models resulting from this procedure.

The MESA results were obtained from AMP 2.0,[15] which originally used models from the Aarhus stellar evolution and pulsation codes (J. Christensen-Dalsgaard 2008a, 2008b). The AMP code was released in 2009 (T. S. Metcalfe et al. 2009; M. Woitaszek et al. 2009), and several minor revisions followed as the quality of asteroseismic data from the Kepler mission gradually improved (S. Mathur et al. 2012; T. S. Metcalfe et al. 2014; O. L. Creevey et al. 2017). The first major revision coupled the same optimization method to the MESA (B. Paxton et al. 2011) and GYRE (R. H. D. Townsend & S. A. Teitler 2013) codes. Although most of the input physics in the new version of AMP were chosen to be the same as in the previous version, there were two major updates that addressed the dominant sources of systematic error in the analysis of Kepler data sets. First, although the Aarhus models included diffusion and settling of helium (Michaud & Proffitt 1993), the treatment of heavier elements was numerically unstable. The MESA models include diffusion and settling of both helium and heavier elements (A. A. Thoul et al. 1994). Second, the original version of AMP included an empirical correction for inadequate modeling of near-surface layers (H. Kjeldsen et al. 2008), while the updated version uses a physically motivated correction that has now become the standard in the field (W. H. Ball & L. Gizon 2014).

The asteroseismic radius, mass, and age of β Hyi from the YREC and MESA modeling procedures are listed in Table 2. The consistency of the asteroseismic properties from these two independent model grids and fitting methodologies suggests that they are robust at the indicated level of precision.

4. Interpretation

4.1. Rotational Evolution Modeling

We performed rotational evolution modeling following a procedure similar to that described in T. S. Metcalfe et al. (2020). We used a tracer code that computes the torque on the star given the braking law of J. L. van Saders et al. (2016) and the stellar structure as a function of age. We utilized two different evolutionary codes to predict the stellar structure. The

[15] https://github.com/travismetcalfe/AMP2

Table 2
Properties of the Solar-type Subgiant β Hyi

	β Hyi	Source
$T_{\rm eff}$ (K)	5872 ± 74	(1)
[Fe/H] (dex)	-0.10 ± 0.09	(2)
log g (dex)	3.84 ± 0.08	(2)
$B - V$ (mag)	0.618	(3)
log $R'_{\rm HK}$ (dex)	-4.996	(3)
$P_{\rm cyc}$ (yr)	$12.0^{+3.0}_{-1.7}$	(4)
$P_{\rm rot}$ (days)	23.0 ± 2.8	(5)
Luminosity ($L_\odot$)	3.45 ± 0.10	(6)
YREC Radius ($R_\odot$)	1.831 ± 0.009	(7)
MESA Radius ($R_\odot$)	1.840 ± 0.032	(7)
YREC Mass ($M_\odot$)	1.107 ± 0.009	(7)
MESA Mass ($M_\odot$)	1.127 ± 0.054	(7)
YREC Age (Gyr)	6.46 ± 0.13	(7)
MESA Age (Gyr)	6.26 ± 0.57	(7)

References: (1) J. R. North et al. (2007); (2) H. Bruntt et al. (2010); (3) T. J. Henry et al. (1996); (4) T. S. Metcalfe et al. (2007); (5) Section 2.2; (6) Section 2.3; (7) Section 3.2.

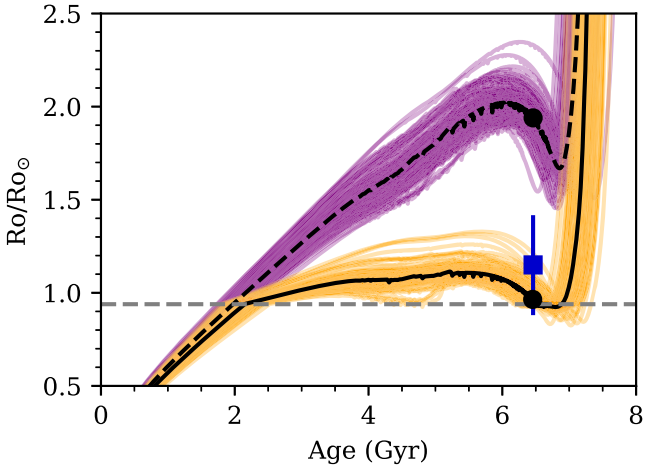

Figure 5. Evolution of the Rossby number for β Hyi in the YREC model grid, with samples drawn from the posterior of the standard spin-down model (purple curves) and from the WMB model (orange curves). The value of $\rm Ro_{crit}$ is shown as a gray dashed line, while the best-fit value of the Rossby number is shown as a circle for both braking-law prescriptions. The actual position of β Hyi (assuming the local convective turnover time of the best-fit model but the measured period and age) is shown as a blue square with an error bar.

first was a YREC model grid that assumed a chemical enrichment law for helium as a function of metallicity but a free mixing-length parameter for convection, with input physics described in T. S. Metcalfe et al. (2020). The second grid was constructed with MESA, tuned to match the input physics of AMP 2.0 (T. S. Metcalfe et al. 2023c) and described in detail by N. Saunders et al. (2024). This grid allowed both the mixing length and helium to be free parameters.

For the braking law, we adopted the form of J. L. van Saders et al. (2016) and the calibration of N. Saunders et al. (2024), which determined best-fit braking-law parameters using a Bayesian hierarchical framework to model both individual asteroseismic and open cluster system parameters, as well as the parameters of the braking law itself, which were assumed to be the same for all stars in the sample. We adopted their critical Rossby number $\rm Ro_{crit} = 0.94 \pm 0.04\,Ro_\odot$ ($\rm Ro_\odot = 2.33$) and braking normalization $f_K = 7.64$ for the YREC model grid and $\rm Ro_{crit} = 0.91 \pm 0.03\,Ro_\odot$ ($\rm Ro_\odot = 2.05$) and $f_K = 5.46 \pm 0.51$ for the MESA model grid. We also adopted their fits of the standard spin-down model to the data (without WMB), where $f_{K,\rm YREC} = 8.55$ and $f_{K,\rm MESA} = 6.11$.

For both model grids, we used $T_{\rm eff}$, [Fe/H], $L_{\rm bol}$, and their 1σ uncertainties as surface constraints. We adopted a wide Gaussian prior on mass ($\sigma = 0.5\,M_\odot$) from asteroseismology and bulk starting metallicity ($\sigma = 0.3$ dex) but a tight asteroseismic prior on age (6.46 ± 0.13 Gyr for the YREC grid and 6.26 ± 0.57 Gyr for the MESA grid). This was done to help mitigate the "overcounting" of constraints: the asteroseismic modeling adopted the measured surface properties as constraints, so knowledge of them is already reflected in the asteroseismic mass. Age is weakly constrained by measurements of $T_{\rm eff}$, [Fe/H], and $L_{\rm bol}$ but very tightly constrained by the small frequency separation and the avoided crossing. In this sense, the asteroseismic age is more independent of the surface constraints than the mass. For this reason, we adopted the tight prior on the asteroseismic age but only very broad priors on other asteroseismic properties. We assumed a mixing-length prior of 1.7 ± 0.2 bounded [1.4, 2.0] for both grids. In the YREC grid, the initial helium abundance was treated with a chemical enrichment law; in the MESA grid it was free to vary and assigned a prior of 0.26 ± 0.10, bounded [0.22, 0.28]. We considered values below the primordial helium abundance to allow for the possibility of systematic errors in the stellar models and to avoid truncating the posterior probability distributions. Note that the measured rotation period from Section 2.2 was not used as an input constraint but only as a consistency check with the predictions from two different sets of braking models.

For the YREC standard spin-down model, we adopt the best-fit N. Saunders et al. (2024) braking-law parameters without uncertainties and predict a rotation period of 39^{+6}_{-7} days. For the WMB model, we predict a period of 19.4 ± 3.5 days. In the MESA grid, we use the neural network framework of N. Saunders et al. (2024) to predict periods using No-U-Turn Sampling (M. D. Hoffman et al. 2014), which is a modified Hamiltonian Markov Chain Monte Carlo algorithm. The adopted $\rm Ro_{crit}$ and f_K were treated as parameters with tight Gaussian priors given by their quoted uncertainties in N. Saunders et al. (2024). The standard spin-down model predicts a rotation period of 35^{+11}_{-8} days, while the WMB model predicts 19^{+5}_{-4} days. These values are substantially unchanged if we adopt the asteroseismic properties of the lower-mass model from MESA, with the same wide mass prior now centered at $1.059\,M_\odot$ and a tight age prior of 6.10 ± 0.19 Gyr.

In both grids, despite differing model physics and assumptions about the helium, the WMB model predicts a period consistent with that recovered from the current TESS photometry, albeit slightly shorter. As found by N. Saunders et al. (2024), this is a common pattern in more evolved stars and may arise from our simplified braking prescription. Beyond $\rm Ro_{crit}$, magnetic braking is assumed to cease entirely, but in reality, there may still be some minimal spin-down that subtly slows the rotation (along with the increasing moment of inertia) during the latter half of the main-sequence lifetime. Regardless, standard spin-down models predict much longer rotation periods that are inconsistent with the observations.

Figure 5 illustrates the evolution of the Rossby number in the YREC model grid as a function of stellar age, with the current observed position of β Hyi marked and curves for both the standard spin-down (purple) and WMB (orange) cases. Standard spin-down models predict a relatively large Rossby

number by the age of β Hyi, while WMB models predict a Rossby number much closer to the solar value, where stellar activity cycles are most prominent (R. Egeland 2017).

4.2. The Born-again Dynamo Phenomenon

The properties of β Hyi provide a second example of the "born-again" dynamo phenomenon that was previously suggested to explain the cycle in 94 Aqr Aa (T. S. Metcalfe et al. 2020). In that scenario, β Hyi started as an F-type star on the main sequence, where it probably had a short-period activity cycle like ι Hor (T. S. Metcalfe et al. 2010). The cycle would gradually grow longer as the rotation rate slowed due to magnetic braking over the next $\sim$2 Gyr, until it reached the critical Rossby number for the onset of WMB. During the second half of its main-sequence lifetime, the rotation rate would remain almost constant, while the cycle would grow longer and weaker before disappearing entirely (T. S. Metcalfe & J. van Saders 2017). However, when hydrogen shell burning began and the star expanded and cooled onto the subgiant branch, the longer turnover time in the deeper convection zone would overwhelm the longer rotation period from conservation of angular momentum. For stars slightly more massive than the Sun, these evolutionary effects can push the Rossby number back below $\mathrm{Ro_{crit}}$, reinvigorating the large-scale dynamo and briefly sustaining an activity cycle once again before ascending the red giant branch. The current position of β Hyi in Figure 5 generally supports this evolutionary scenario, which only returns below $\mathrm{Ro_{crit}}$ in the WMB scenario.

The activity cycle of 94 Aqr Aa is much more prominent in Ca HK than the cycle in β Hyi. The IUE data for β Hyi show a magnetic maximum in 1986.9, followed by a rise toward the subsequent maximum in late 1998 (top panel of Figure 1). The Ca HK observations from mid-2007 to 2013 span the next predicted maximum in late 2010 and show a slightly higher mean activity level during the 2010 season followed by a gradual decline from 2011 to 2012 (bottom panel of Figure 1). Earlier Ca HK measurements during the cycle minimum in 1993 showed a similar range ($S = 0.151$–0.171; T. J. Henry et al. 1996), so the cycle amplitude in the optical appears to be substantially smaller than in the ultraviolet. This is a consequence of the larger dynamic range for magnetic variability at higher energies, which also explains the clear X-ray cycle in α Cen A (T. Ayres 2023) that has not been detected in the optical. These stars might have been classified as "flat activity" targets from their optical data alone, but the availability of higher-energy observations revealed their cycles. By contrast, Mount Wilson observations of 94 Aqr Aa show a robust cycle in Ca HK (T. S. Metcalfe et al. 2020).

The difference between the Ca HK variability of β Hyi and 94 Aqr Aa may be a consequence of their relative Rossby numbers. Because rotation and activity are strongly coupled prior to the onset of WMB, $\mathrm{Ro_{crit}}$ can be converted into a critical activity level ($\log R'_{\mathrm{HK}} \approx -4.95$; A. Brandenburg et al. 2017). For any given star, this critical activity level corresponds to a specific Mount Wilson S index (S_{crit}), which depends on the $B-V$ color (R. W. Noyes et al. 1984). For β Hyi this value is $S_{\mathrm{crit}} = 0.165$, which falls above most of the observations shown in the bottom panel of Figure 1. By contrast, the critical activity level for 94 Aqr Aa is $S_{\mathrm{crit}} = 0.18$, which falls within the range of variability in the Mount Wilson measurements ($S = 0.136$–0.196; T. S. Metcalfe et al. 2020). Thus, the cycle is weaker in β Hyi because it is closer to $\mathrm{Ro_{crit}}$, while 94 Aqr Aa is well below $\mathrm{Ro_{crit}}$ and has a stronger cycle.

5. Summary and Discussion

We have used two months of TESS observations to characterize the solar-type subgiant β Hyi and investigate the nature of its activity cycle (Figure 1). We extracted a custom light curve from the data, reducing the noise by a factor of 2 (Section 2.1) and enabling the first direct measurement of the rotation period (Section 2.2). Analysis of the solar-like oscillations (Section 3.1) identified 23 individual frequencies for detailed asteroseismic modeling (Table 1), yielding precise estimates of the stellar radius, mass, and age (Section 3.2). The resulting stellar properties (Table 2) provided inputs for rotational evolution modeling (Section 4.1), showing that the rotation period of β Hyi is consistent with WMB. In addition, the current Rossby number of β Hyi is comparable to 94 Aqr Aa (Figure 5), which may help explain the existence of its activity cycle. We conclude that changes in stellar structure on the subgiant branch can reinvigorate the large-scale dynamo and briefly sustain magnetic activity cycles (Section 4.2), a phenomenon that was originally suggested to explain the cycle in 94 Aqr Aa (T. S. Metcalfe et al. 2020) and can best be understood within the WMB scenario.

The critical Rossby number for the onset of WMB ($\mathrm{Ro_{crit}}$) might also represent a threshold beyond which large-scale dynamos have difficulty driving cycles (B. Tripathi et al. 2021). As an illustration of the empirical evidence for this idea, the long-term activity records from A. C. Baum et al. (2022) are shown for three stars in Figure 6. Observations from the Mount Wilson survey are shown with black plus symbols, those from Keck are shown with blue crosses, and the critical activity level for each star (S_{crit}; see Section 4.2) is indicated with a magenta dashed line. The K0 dwarf σ Dra (top panel) is approaching $\mathrm{Ro_{crit}}$ and shows a clear activity cycle with a minimum level comparable to S_{crit}. The less active K2 dwarf HD 166620 (middle panel) initially shows a clear cycle with a mean activity level similar to S_{crit} before the star apparently enters a magnetic grand minimum (J. K. Luhn et al. 2022). This type of intermittency is predicted to become more frequent and more prolonged as the mean activity level continues to decline with age (V. Vashishth et al. 2023). During this phase, active regions that emerge with unusual properties (e.g., violating Hale's polarity law or Joy's tilt angle law) can switch the dynamo between the cycling and noncycling states (M. Nagy et al. 2017). Eventually, continued evolution pushes the mean activity level so far below S_{crit} that even the most extreme active regions can no longer shift the dynamo between these states, and cycles disappear entirely as in the G7 subgiant 31 Aql (bottom panel). Most of the "flat activity" stars in the Mount Wilson survey appear to be in this permanently low activity regime (R. Egeland 2017).

Recent direct estimates of the wind-braking torque in old solar-type stars have revealed an unexpected decline in the large-scale magnetic field as well as the mass-loss rate (T. S. Metcalfe et al. 2021, 2022, 2023b, 2024), and β Hyi can connect these effects to underlying changes in the stellar dynamo. We suggest that $\mathrm{Ro_{crit}}$ corresponds to a rotation rate that is too slow to imprint substantial Coriolis forces on the global convective patterns.[16] Consequently, related properties

[16] Note that the onset of WMB at $\mathrm{Ro_{crit}}$ may prevent most main-sequence stars from reaching the higher Rossby numbers above $\sim$1.1 $\mathrm{Ro_\odot}$ that are required in global convection simulations to generate antisolar differential rotation (Q. Noraz et al. 2024), so stars that rotate faster at the pole and slower at the equator are primarily expected on the red giant branch.

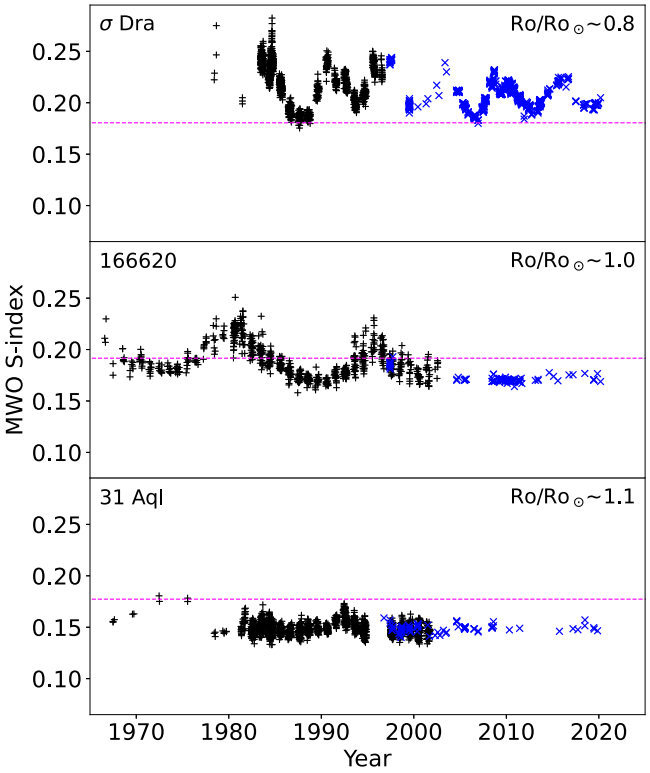

Figure 6. Evolution of stellar activity cycles through the critical activity level that corresponds to Ro_{crit} (magenta dashed lines). Mount Wilson data are shown with black plus symbols, while Keck data are shown with blue crosses (A. C. Baum et al. 2022). Close to the onset of WMB, the critical activity level is near cycle minimum as in σ Dra (top). As the mean activity level decreases with age, the cycle can develop intermittency as in HD 166620 (middle). Continued evolution pushes the mean activity level permanently below the critical value, and cycles disappear entirely as in 31 Aql (bottom).

such as differential rotation, meridional circulation, and tilted active region emergence begin to be disrupted. The loss of shear from differential rotation weakens the Ω effect, inhibiting the production of buoyant magnetic loops within the convection zone and yielding shallower tilt angles when they ultimately emerge. As the near-surface convection gradually shreds bipolar magnetic regions, the shallower tilt and weaker differential rotation leads to enhanced cancellation of magnetic flux, and the weaker meridional circulation transports less of the residual flux toward the polar regions to seed the regeneration of a large-scale field. This leads to a downward spiral of both flux emergence and the production of a large-scale magnetic field on stellar evolutionary timescales. With a higher fraction of the remaining field concentrated in smaller spatial scales, the diminished large-scale field weakens magnetic braking (V. Réville et al. 2015; C. Garraffo et al. 2016; V. See et al. 2019), and the increased magnetic complexity throttles the stellar wind from the smaller area with open magnetic field lines (C. Garraffo et al. 2015; M. Shoda et al. 2023), as suggested by the recent wind-braking estimates.

Future observations of β Hyi will enable a direct estimate of the wind-braking torque during the "born-again" dynamo phase, providing new constraints on the late stages of magnetic stellar evolution. Such an estimate will require spectropolarimetry to constrain the large-scale magnetic morphology (A. J. Finley & S. P. Matt 2018), Lyα analysis or an X-ray flux to estimate the mass-loss rate (B. E. Wood et al. 2021), the rotation period determined in Section 2.2, and the asteroseismic radius and mass determined in Section 3.2. Spectropolarimetry of β Hyi was obtained in 2024 July with HARPSpol, and Lyα measurements have been approved for the Hubble Space Telescope, so we should soon learn how the resurgence of a stellar activity cycle affects the current rate of angular momentum loss in this evolved subgiant.

Acknowledgments

We would like to thank Axel Brandenburg, Paul Charbonneau, and Ricky Egeland for helpful discussions. This paper includes data collected with the TESS mission, obtained from the Mikulski Archive for Space Telescopes at the Space Telescope Science Institute (STScI). The specific observations analyzed can be accessed via doi:10.17909/g809-wf30. Funding for the TESS mission is provided by the NASA Explorer Program. STScI is operated by the Association of Universities for Research in Astronomy, Inc., under NASA contract NAS 526555. T.S.M. acknowledges support from NASA grant 80NSSC22K0475. Computational time at the Texas Advanced Computing Center was provided through XSEDE allocation TG-AST090107. D.H. acknowledges support from the Alfred P. Sloan Foundation, NASA (80NSSC22K0303, 80NSSC23K0434, 80NSSC23K0435), and the Australian Research Council (FT200100871). R.A.G. acknowledges support from the PLATO and SoHO/GOLF grants of the Centre National D'Études Spatiales. S.N.B. acknowledges support from PLATO ASI-INAF agreement no. 2022-28-HH.0 "PLATO Fase D". M.B.N. acknowledges support from the UK Space Agency. J.M.J.O. acknowledges support from the NASA Hubble Fellowship grant HST-HF2-51517.001, awarded by STScI. N.S. acknowledges support from the NSF Graduate Research Fellowship Program under grant Nos. 1842402 and 2236415. This research benefited from discussions at the workshop "Solar and Stellar Dynamos: A New Era", hosted and supported by the International Space Science Institute in Bern, Switzerland.

ORCID iDs

Travis S. Metcalfe https://orcid.org/0000-0003-4034-0416
Jennifer L. van Saders https://orcid.org/0000-0002-4284-8638
Daniel Huber https://orcid.org/0000-0001-8832-4488
Derek Buzasi https://orcid.org/0000-0002-1988-143X
Rafael A. García https://orcid.org/0000-0002-8854-3776
Keivan G. Stassun https://orcid.org/0000-0002-3481-9052
Sarbani Basu https://orcid.org/0000-0002-6163-3472
Sylvain N. Breton https://orcid.org/0000-0003-0377-0740
Zachary R. Claytor https://orcid.org/0000-0002-9879-3904
Enrico Corsaro https://orcid.org/0000-0001-8835-2075
Martin B. Nielsen https://orcid.org/0000-0001-9169-2599
J. M. Joel Ong https://orcid.org/0000-0001-7664-648X
Nicholas Saunders https://orcid.org/0000-0003-2657-3889
Amalie Stokholm https://orcid.org/0000-0002-5496-365X
Timothy R. Bedding https://orcid.org/0000-0001-5222-4661

References

Aguirre Børsen-Koch, V., Rørsted, J. L., Justesen, A. B., et al. 2022, MNRAS, 509, 4344
Aigrain, S., Llama, J., Ceillier, T., et al. 2015, MNRAS, 450, 3211

Aizenman, M., Smeyers, P., & Weigert, A. 1977, A&A, 58, 41
Appourchaux, T., Benomar, O., Gruberbauer, M., et al. 2012, A&A, 537, A134
Ayres, T. 2023, AJ, 166, 212
Baliunas, S. L., Donahue, R. A., Soon, W. H., et al. 1995, ApJ, 438, 269
Ball, W. H., & Gizon, L. 2014, A&A, 568, A123
Baum, A. C., Wright, J. T., Luhn, J. K., & Isaacson, H. 2022, AJ, 163, 183
Bedding, T. R., Butler, R. P., Kjeldsen, H., et al. 2001, ApJL, 549, L105
Bedding, T. R., Kjeldsen, H., Arentoft, T., et al. 2007, ApJ, 663, 1315
Benomar, O., Bedding, T. R., Stello, D., et al. 2012, ApJL, 745, L33
Böhm-Vitense, E. 2007, ApJ, 657, 486
Brandão, I. M., Doğan, G., Christensen-Dalsgaard, J., et al. 2011, A&A, 527, A37
Brandenburg, A., Mathur, S., & Metcalfe, T. S. 2017, ApJ, 845, 79
Breton, S. N., García, R. A., Ballot, J., Delsanti, V., & Salabert, D. 2022, A&A, 663, A118
Bruntt, H., Bedding, T. R., Quirion, P. O., et al. 2010, MNRAS, 405, 1907
Carrier, F., Bouchy, F., Kienzle, F., et al. 2001, A&A, 378, 142
Ceillier, T., Tayar, J., Mathur, S., et al. 2017, A&A, 605, A111
Ceillier, T., van Saders, J., García, R. A., et al. 2016, MNRAS, 456, 119
Christensen-Dalsgaard, J. 2008a, Ap&SS, 316, 13
Christensen-Dalsgaard, J. 2008b, Ap&SS, 316, 113
Corsaro, E., & De Ridder, J. 2014, A&A, 571, A71
Corsaro, E., McKeever, J. M., & Kuszlewicz, J. S. 2020, A&A, 640, A130
Creevey, O. L., Metcalfe, T. S., Schultheis, M., et al. 2017, A&A, 601, A67
Demarque, P., Guenther, D. B., Li, L. H., Mazumdar, A., & Straka, C. W. 2008, Ap&SS, 316, 31
Di Mauro, M. P., Christensen-Dalsgaard, J., & Paternò, L. 2003, Ap&SS, 284, 229
Doğan, G., Brandão, I. M., Bedding, T. R., et al. 2010, Ap&SS, 328, 101
Dravins, D., Linde, P., Ayres, T. R., et al. 1993a, ApJ, 403, 412
Dravins, D., Linde, P., Fredga, K., & Gahm, G. F. 1993b, ApJ, 403, 396
Dravins, D., Lindegren, L., Nordlund, A., & Vandenberg, D. A. 1993c, ApJ, 403, 385
Dravins, D., Lindegren, L., & Vandenberg, D. A. 1998, A&A, 330, 1077
Edmonds, P. D., & Cram, L. E. 1995, MNRAS, 276, 1295
Egeland, R. 2017, PhD thesis, Montana State Univ.
Egeland, R. 2018, ApJ, 866, 80
Elad, M., Starck, J.-L., Querre, P., & Donoho, D. L. 2005, Appl. Comput. Harmon. Anal., 19, 340
Fernandes, J., & Monteiro, M. J. P. F. G. 2003, A&A, 399, 243
Finley, A. J., & Matt, S. P. 2018, ApJ, 854, 78
Frandsen, S. 1987, A&A, 181, 289
Gaia Collaboration, Brown, A. G. A., Vallenari, A., et al. 2021, A&A, 649, A1
García, R. A., Ceillier, T., Salabert, D., et al. 2014a, A&A, 572, A34
García, R. A., Gourvès, C., Santos, A. R. G., et al. 2023, A&A, 679, L12
García, R. A., Mathur, S., Pires, S., et al. 2014b, A&A, 568, A10
García, R. A., Régulo, C., Samadi, R., et al. 2009, A&A, 506, 41
Garraffo, C., Drake, J. J., & Cohen, O. 2015, ApJ, 813, 40
Garraffo, C., Drake, J. J., & Cohen, O. 2016, A&A, 595, A110
Handberg, R., & Campante, T. L. 2011, A&A, 527, A56
Henry, T. J., Soderblom, D. R., Donahue, R. A., & Baliunas, S. L. 1996, AJ, 111, 439
Hoffman, M. D., Gelman, A., et al. 2014, J. Mach. Learn. Res., 15, 1593, http://jmlr.org/papers/v15/hoffman14a.html
Huber, D., White, T. R., Metcalfe, T. S., et al. 2022, AJ, 163, 79
Jenkins, J. M., Twicken, J. D., McCauliff, S., et al. 2016, Proc. SPIE, 9913, 99133E
Kjeldsen, H., Bedding, T. R., & Christensen-Dalsgaard, J. 2008, ApJL, 683, L175
Lam, K. W. F., Csizmadia, S., Astudillo-Defru, N., et al. 2021, Sci, 374, 1271
Luhn, J. K., Wright, J. T., Henry, G. W., Saar, S. H., & Baum, A. C. 2022, ApJL, 936, L23
Mathur, S., García, R. A., Régulo, C., et al. 2010, A&A, 511, A46
Mathur, S., Metcalfe, T. S., Woitaszek, M., et al. 2012, ApJ, 749, 152
McQuillan, A., Aigrain, S., & Mazeh, T. 2013, MNRAS, 432, 1203
Mermilliod, J. C. 2006, yCat, II/168
Metcalfe, T. S., Basu, S., Henry, T. J., et al. 2010, ApJL, 723, L213
Metcalfe, T. S., Buzasi, D., Huber, D., et al. 2023a, AJ, 166, 167
Metcalfe, T. S., Creevey, O. L., & Christensen-Dalsgaard, J. 2009, ApJ, 699, 373
Metcalfe, T. S., Creevey, O. L., Doğan, G., et al. 2014, ApJS, 214, 27
Metcalfe, T. S., Dziembowski, W. A., Judge, P. G., & Snow, M. 2007, MNRAS, 379, L16
Metcalfe, T. S., Finley, A. J., Kochukhov, O., et al. 2022, ApJL, 933, L17
Metcalfe, T. S., Strassmeier, K. G., Ilyin, I. V., et al. 2023b, ApJL, 948, L6
Metcalfe, T. S., Strassmeier, K. G., Ilyin, I. V., et al. 2024, ApJL, 960, L6
Metcalfe, T. S., Townsend, R. H. D., & Ball, W. H. 2023c, RNAAS, 7, 164
Metcalfe, T. S., & van Saders, J. 2017, SoPh, 292, 126
Metcalfe, T. S., van Saders, J. L., Basu, S., et al. 2020, ApJ, 900, 154
Metcalfe, T. S., van Saders, J. L., Basu, S., et al. 2021, ApJ, 921, 122
Michaud, G., & Proffitt, C. R. 1993, in ASP Conf. Ser. 40, Inside the Stars, ed. Weiss W. W. & Baglin A. (San Francisco, CA: ASP), 246
Mosser, B., Elsworth, Y., Hekker, S., et al. 2012, A&A, 537, A30
Nagy, M., Lemerle, A., Labonville, F., Petrovay, K., & Charbonneau, P. 2017, SoPh, 292, 167
Nielsen, M. B., Ball, W. H., Standing, M. R., et al. 2020, A&A, 641, A25
Nielsen, M. B., Davies, G. R., Ball, W. H., et al. 2021, AJ, 161, 62
Noraz, Q., Brun, A. S., & Strugarek, A. 2024, A&A, 684, A156
North, J. R., Davis, J., Bedding, T. R., et al. 2007, MNRAS, 380, L80
Noyes, R. W., Hartmann, L. W., Baliunas, S. L., Duncan, D. K., & Vaughan, A. H. 1984, ApJ, 279, 763
Olmedo, M., Chávez, M., Bertone, E., & De la Luz, V. 2013, PASP, 125, 1436
Paunzen, E. 2015, A&A, 580, A23
Paxton, B., Bildsten, L., Dotter, A., et al. 2011, ApJS, 192, 3
Pires, S., Mathur, S., García, R. A., et al. 2015, A&A, 574, A18
Réville, V., Brun, A. S., Matt, S. P., Strugarek, A., & Pinto, R. F. 2015, ApJ, 798, 116
Ricker, G. R., Winn, J. N., Vanderspek, R., et al. 2014, Proc. SPIE, 9143, 914320
Santos, A. R. G., Breton, S. N., Mathur, S., & García, R. A. 2021, ApJS, 255, 17
Santos, A. R. G., García, R. A., Mathur, S., et al. 2019, ApJS, 244, 21
Saunders, N., van Saders, J. L., Lyttle, A. J., et al. 2024, ApJ, 962, 138
See, V., Matt, S. P., Finley, A. J., et al. 2019, ApJ, 886, 120
Shoda, M., Cranmer, S. R., & Toriumi, S. 2023, ApJ, 957, 71
Starck, J.-L., & Murtagh, F. 2006, Astronomical Image and Data Analysis (Berlin: Springer)
Stassun, K. G., Collins, K. A., & Gaudi, B. S. 2017, AJ, 153, 136
Stassun, K. G., Corsaro, E., Pepper, J. A., & Gaudi, B. S. 2018, AJ, 155, 22
Stassun, K. G., & Torres, G. 2016, ApJL, 831, L6
Stassun, K. G., & Torres, G. 2021, ApJL, 907, L33
Thoul, A. A., Bahcall, J. N., & Loeb, A. 1994, ApJ, 421, 828
Torrence, C., & Compo, G. P. 1998, BAMS, 79, 61
Torres, G., Fischer, D. A., Sozzetti, A., et al. 2012, ApJ, 757, 161
Townsend, R. H. D., & Teitler, S. A. 2013, MNRAS, 435, 3406
Tripathi, B., Nandy, D., & Banerjee, S. 2021, MNRAS, 506, L50
van Saders, J. L., Ceillier, T., Metcalfe, T. S., et al. 2016, Natur, 529, 181
Vashishth, V., Karak, B. B., & Kitchatinov, L. 2023, MNRAS, 522, 2601
Woitaszek, M., Metcalfe, T., & Shorrock, I. 2009, in Proc. of the 5th Grid Computing Environments Workshop (New York: ACM Press), 1
Wood, B. E., Müller, H.-R., Redfield, S., et al. 2021, ApJ, 915, 37